Exploring a Global Multiresolution Modeling Approach Using Aquaplanet Simulations*

SARA A. RAUSCHER AND TODD D. RINGLER

Fluid Dynamics and Solid Mechanics Group, Theoretical Division, Los Alamos National Laboratory, Los Alamos, New Mexico

WILLIAM C. SKAMAROCK

Mesoscale and Microscale Meteorology Division, National Center for Atmospheric Research,+ Boulder, Colorado

ARTHUR A. MIRIN

Center for Applied Scientific Computing, Lawrence Livermore National Laboratory, Livermore, California

(Manuscript received 20 March 2012, in final form 5 September 2012)

ABSTRACT

Results from aquaplanet experiments performed using the Model for Prediction across Scales (MPAS) hydrostatic dynamical core implemented within the Department of Energy (DOE)–NCAR Community Atmosphere Model (CAM) are presented. MPAS is an unstructured-grid approach to climate system modeling that supports both quasi-uniform and variable-resolution meshing of the sphere based on conforming grids. Using quasi-uniform simulations at resolutions of 30, 60, 120, and 240 km, the authors evaluate the performance of CAM-MPAS via its kinetic energy spectra, general circulation, and precipitation characteristics. By analyzing an additional variable-resolution simulation with grid spacing that varies from 30 km in a spherical, continental-sized equatorial region to 240 km elsewhere, the CAM-MPAS's potential for use as a regional climate simulation tool is explored.

Similar to other quasi-uniform aquaplanet simulations, tropical precipitation increases with resolution, indicating the resolution sensitivity of the physical parameterizations. Comparison with the finite volume (FV) dynamical core suggests a weaker tropical circulation in the CAM-MPAS simulations, which is evident in reduced tropical precipitation and a weaker Hadley circulation. In the variable-resolution simulation, the kinetic energy spectrum within the high-resolution region closely resembles the quasi-uniform 30-km simulation, indicating a robust simulation of the fluid dynamics. As suggested by the quasi-uniform simulations, the CAM4 physics behave differently in the high and low resolution regions. A positive precipitation anomaly occurs on the western edge of the high-resolution region, exciting a Gill-type response; this zonal asymmetry represents the errors incurred in a variable resolution setting. When paired with a multiresolution mesh, the aquaplanet test case offers an exceptional opportunity to examine the response of physical parameterizations to grid resolution.

1. Introduction

The lack of reliable regional climate projections represents one of the largest gaps in climate change science. While some confidence exists in projections of global and large-scale climate change (Meehl et al. 2007), challenges remain in producing consistent projections at regional and local scales. Traditionally, three dynamical modeling methods have been used to obtain regional climate information: limited-area (or regional) climate models (RCMs) driven by reanalysis or GCM boundary conditions, usually in one-way nesting mode; high-resolution global models; and variable-resolution techniques. Regional climate models offer high resolution at reduced cost compared to high-resolution global modeling, but issues such as ill-posed boundary conditions, mismatches between the driving GCM and the RCM dynamics and physics, and the lack of

* Lawrence Livermore National Laboratory Report LLNL-JRNL-538911.

+ The National Center for Atmospheric Research is sponsored by the National Science Foundation.

Corresponding author address: Sara A. Rauscher, Theoretical Division, Los Alamos National Laboratory, Los Alamos, NM 87545.
E-mail: rauscher@lanl.gov

DOI: 10.1175/JCLI-D-12-00154.1

''upscale'' effects continue to call into question the validity of RCMs; see reviews in Giorgi and Mearns (1991), Giorgi and Mearns (1999), and Laprise et al. (2008). Progress toward global high-resolution simulations has been stymied by high computational costs, although quasi-uniform grids that do not require polar filtering and that scale well on newer petascale machines are beginning to offer relief (Taylor et al. 2008). However, widespread use of global high-resolution simulations is undoubtedly years away owing to demands for increasing model complexity and the computing resources necessary to carry out these grand challenge simulations. Variable resolution approaches offer a compromise, with reduced computational cost compared to global high-resolution simulations and internal consistency and interactions between the large scale and regional scales that are generally absent in traditional RCMs.

Despite the potential appeal of variable-resolution climate model simulations, relatively few examples exist, especially in comparison to traditional RCM studies, and the few examples reported in the literature have been limited to the use of stretched-grid or conformal mapping approaches (Fox-Rabinovitz et al. 1997; Déqué et al. 2005; Lorant and Royer 2001; Fox-Rabinovitz et al. 2006). In both of these approaches, the mesh is deformed through a continuous mapping and, as a result, the mesh is topologically unchanged as the resolution varies. Thus, increased resolution in one region comes at the expense of decreased resolution in another region. This ''stretching'' factor between the coarse-resolution and fine-resolution regions is directly related to simulation quality, as large differences between the coarse and fine resolution regions have the potential to degrade the simulation. For example, Lorant and Royer (2001) found that equatorial waves were slowed down or even reversed in the coarse region of a variable-resolution aquaplanet simulation. Further, stretched-grid approaches may have increased resolution in one region only.

A new multiscale modeling approach, the Model for Prediction across Scales (MPAS), overcomes the limitations of continuous mesh stretching found in previous variable-resolution modeling approaches through the use of spherical centroidal Voronoi tessellations (SCVTs)[1] (Du et al. 1999; Ringler et al. 2008). MPAS is amenable to local mesh refinement through the specification of a single scalar density function that results in higher resolution where this density function is large and lower resolution where this density function is small (see, e.g., Ju et al. 2011). Meshes can be configured with multiple high-resolution regions, and resolution increases in one region do not need to be balanced by coarser resolution elsewhere. The underlying theory of SCVTs is robust in the sense that we know with high certainty a priori what the grid resolution will be at every location on the sphere given the scalar density function and the total number of grid cells.

These multiresolution SCVTs are paired with a recent generalization of the C-grid staggering shown to be applicable to a wide variety of meshes (Thuburn et al. 2009; Ringler et al. 2010). This generalization guarantees a realistic simulation of geostrophic adjustment (Thuburn et al. 2009), exact mass, tracer, and potential vorticity conservation, along with energy conservation to within time-truncation error (Ringler et al. 2010). This modeling approach has been evaluated based on the standard shallow-water test case suite of Williamson et al. (1992) using both quasi-uniform (Ringler et al. 2010) and variable resolution (Ringler et al. 2011) meshes. When configured with quasi-uniform meshes, the rate of convergence is found to be between first and second order, as is typical of finite-volume methods. Both the conservation properties and rate of convergence are unchanged when configured with variable resolution meshes. However, when using variable resolution meshes the solution error in the shallow-water test case suite is controlled by the coarsest region of the global mesh. As a result, the justification for using a global multiresolution mesh cannot rest on a belief that use of variable resolution meshes will result in the formal reduction of solution error associated with the underlying partial differential equation. Rather, justification is more likely to emerge from the ability to directly simulate important phenomena in specific regions of interest. Based on the shallow-water results, the next step in the development of MPAS is to evaluate a primitive-equation, hydrostatic version of the MPAS dynamical core coupled to the Community Atmosphere Model (CAM), and this is the subject of this paper.

Although regional climate modeling efforts have been underway for over two decades (Dickinson et al. 1989), it is unclear which regional climate modeling method provides the most robust results. While suites of idealized test cases are applied as a standard part of GCM development (e.g., Williamson et al. 1992; Held and Suarez 1994; Neale and Hoskins 2000a), regional modeling techniques have not been so rigorously evaluated in idealized settings, or at a minimum that performance has not been well documented. As part of a hierarchical

[1] Voronoi tessellations have been reinvented many times over in the past 150 years, including within the field of climate modeling. These meshes, or variants thereof, are sometimes referred to as ''geodesic grids,'' ''icosahedral grids,'' or ''hexagonal grids.'' For a full review of the history of Voronoi tessellations and their application in climate science, see Ju et al. (2011).

approach to test the veracity of global high-resolution and global variable-resolution simulations for regional modeling applications, we analyze a series of idealized, full-physics aquaplanet test cases produced using CAM version 5 coupled to the new MPAS dynamical core (CAM-MPAS). To provide context for this analysis, the new CAM-MPAS model is compared to the default finite volume (FV) dynamical core (CAM-FV). Aquaplanet simulations are a natural component of a robust hierarchical evaluation framework because they employ idealized boundary forcing by using zonally symmetric sea surface temperatures and equinoctial insolation. Nonetheless, since they also include the full physical parameterization suite present in real-world climate configurations, aquaplanet simulations contain many realistic climate features, such as the intertropical convergence zone (ITCZ), convectively coupled equatorial waves, and tropical cyclones (Neale and Hoskins 2000b). Deficiencies in the approaches to regional climate simulation can be more easily identified in the setting of aquaplanet than in real-world simulations.

Within the context of this simplified aquaplanet setting, we have two goals: 1) to evaluate the basic performance of the MPAS dynamical core in CAM via the kinetic energy spectra, general circulation, and precipitation characteristics and 2) to explore the variable resolution capabilities of MPAS. Simulations are presented with CAM-MPAS using quasi-uniform meshes at approximate grid spacings of 30, 60, 120, and 240 km and compared with simulations using the default finite-volume dynamical core at 0.5° and 2° resolution. Taken together, these simulations allow us to assess the effects of different dynamical cores and increasing resolution. Furthermore, results from these quasi-uniform simulations provide the necessary background and context to evaluate a variable resolution simulation that spans the minimum (30 km) and maximum (240 km) grid spacings considered in our quasi-uniform simulations. In the variable resolution simulation, the high-resolution region is a circular region centered on the equator with a diameter of approximately 6500 km. This area is approximately the size of continental-scale domains typically used with regional climate models, as in the Coordinated Regional Climate Downscaling Experiment (CORDEX) (Giorgi et al. 2009). Notably, this variable resolution mesh has only 10% of the number of grid cells of the quasi-uniform CAM-MPAS 30-km simulation, thus offering the possibility of substantial computational savings. With this idealized variable resolution simulation, we can explore key questions about regional climate simulation: Does the high-resolution region of the variable resolution simulation ''look'' and ''act'' like a quasi-uniform simulation that uses this high resolution everywhere? Are there any upscaled impacts from the high-resolution region to the outer coarse-resolution region? Finally, how do the physical parameterizations react as the fluid enters and exits the high-resolution region?

Section 2 contains a brief overview of CAM physical parameterizations, the MPAS dynamical core, and a description of the aquaplanet configuration. The quasi-uniform simulations are analyzed in section 3 with a focus on the representation of the kinetic energy spectra, general circulation, and model representation of precipitation. Section 4 contains an analysis of variable resolution simulation. Finally, a discussion and conclusions are presented in section 5.

2. Models and experimental design

a. CAM

CAM version 5 is the most recent version of the Community Atmosphere Model; it comprises the atmospheric component of the full Community Earth System Model (CESM). The source code, documentation, and input datasets for the model are available at http://www.cesm.ucar.edu/models/cesm1.0/cam/. Although CAM-MPAS is coupled with CAM version 5.0, we use the CAM version 4 (CAM4) physical parameterizations in our simulations. The default configuration in CAM4 uses 26 vertical levels with a sigma vertical coordinate. Three tracers are advected: specific humidity, cloud liquid, and cloud ice. CAM4 physics are described in detail in Neale et al. (2010), but we list some pertinent details here. CAM4 uses a modified version of the Zhang and McFarlane (1995) convection scheme. A plume ensemble approach is used, wherein if the atmosphere is conditionally unstable, convective-scale updrafts and saturated downdrafts may occur. If sufficient convective available potential energy (CAPE) is present, moist convection occurs. Cloud microphysics are represented by a prognostic, two-moment formulation for cloud droplet and cloud ice with mass and number concentrations following the original parameterization as described by Gettelman et al. (2008). In all of the CAM-MPAS and CAM-FV simulations presented in this study, we use a physics time step of 10 min; we note that aquaplanet experiment results are known to be sensitive to the physics time step in CAM (Williamson and Olson 2003).

b. MPAS-Atmosphere

The MPAS atmospheric dynamical core (MPAS-Atmosphere, referred to here as MPAS-A) is built using

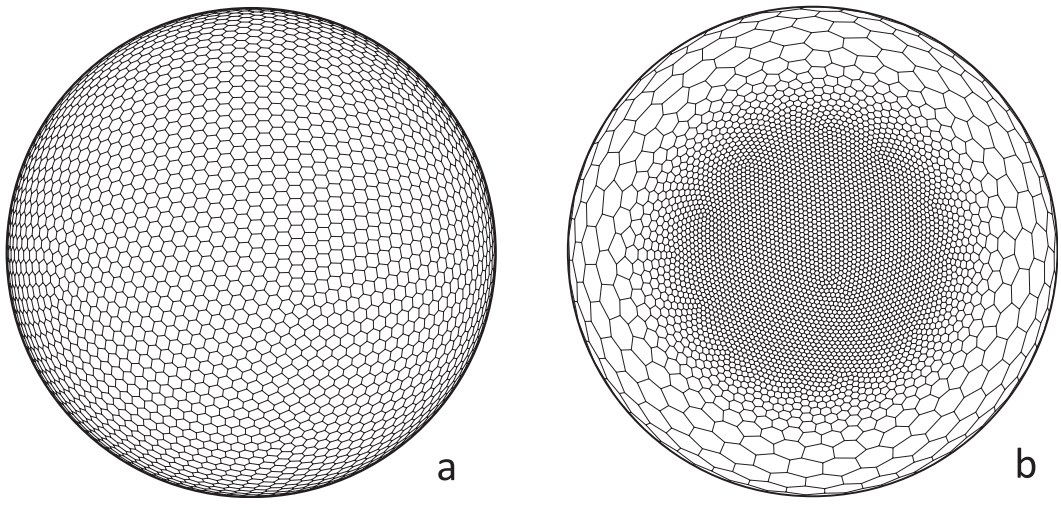

FIG. 1. A (a) quasi-uniform mesh and (b) variable-resolution mesh. Both meshes are shown at resolutions significantly lower than used in the simulations in order to show each grid cell. Both meshes contain the exact same number of grid cells and differ only in the distribution on the sphere.

the horizontal C-grid scheme presented in Thuburn et al. (2009) and Ringler et al. (2010), along with the vertical and time discretization of the Weather Research and Forecasting (WRF) model (Skamarock et al. 2008). A more detailed description of the MPAS-A hydrostatic solver can be found in the appendix in Park et al. (2013). Since CAM-MPAS will be configured with horizontal grid spacings that clearly reside in the hydrostatic regime, the nonhydrostatic option available within WRF is not included in this version of CAM-MPAS. As is standard within CAM, the MPAS-A dynamics and CAM physics are decoupled using a process split approach (i.e., all prognostic variables are updated sequentially by the dynamics and then the physics). This design choice allows for new dynamical cores to be ''ported'' into the CAM modeling system.

MPAS-A can be configured to use any conforming mesh where the line segment connecting cell centers is orthogonal to the edge shared by those two cell centers. While latitude–longitude grids, conformally mapped cubed sphere meshes, Delaunay triangulations, and Voronoi tessellations all meet this criterion, our preference is to use SCVTs, which are the spherical counterpart of Voronoi tessellations. Figure 1 shows a quasi-uniform and variable resolution SCVT. To display the structure of individual grid cells, the meshes are shown at coarser resolutions than we use in our simulations. Both meshes have the exact same number of grid cells but distribute those degrees of freedom differently. The quasi-uniform mesh has essentially the same grid resolution everywhere, while the variable resolution mesh has a grid resolution eight times finer in the high-resolution region than in the low-resolution region. For a full discussion of how these meshes are produced, see Ringler et al. (2011).

In the experiments presented here, MPAS-A is configured with four different quasi-uniform resolution (QUR) meshes with grid spacings of approximately 30, 60, 120, and 240 km and with one variable resolution (VR) mesh, similar to that shown in Fig. 1. The variable resolution mesh has a circular high-resolution region centered on the equator. Grid spacing is approximately 30 km in the high-resolution region from approximately 30°S to 30°N, 30°E to 30°W; the grid spacing then transitions to approximately 240 km over 20° of latitude/longitude, thus bracketing the resolutions of our QUR simulation suite. In the maps and Hovmöller diagrams presented in the discussion of the variable resolution simulation results in section 4, this high-resolution region is outlined in gray.

With one exception, every CAM-MPAS simulation uses the exact same parameter settings. The physics time step, dynamics time step, and moist-physics parameters are unchanged between CAM-MPAS simulations. This is not to imply that these time steps and parameter settings are optimal across the wide range of grid scales investigated here; rather, we hold them constant in order to highlight the sensitivity of the dynamics and physics response to grid resolution. The single parameter that is adjusted based on resolution is the hyperviscosity. In CAM-MPAS, the momentum equation includes a $-\mu\nabla^4\mathbf{u}$ term on the right-hand side to dissipate the downscale cascade of energy and enstrophy. As the grid spacing is decreased, the value of μ is decreased. Boville (1991) and Takahashi et al. (2006) found that an optimal representation of the kinetic energy spectrum, including

TABLE 1. CAM-MPAS aquaplanet simulations.

Dynamical core	Resolution	Number of 2D grid points	Hyperdiffusion	Regridded
MPAS	240 km	10 242	5×10^{15}	FV 1.9×2.5, 96×144
MPAS	120 km	40 962	5×10^{14}	FV 0.9×1.25, 192×288
MPAS	60 km	163 842	5×10^{13}	FV 0.47×0.63, 384×576
MPAS	30 km	655 362	5×10^{12}	FV 0.23×0.31, 768×1152
MPAS	240 to 30 km	65 538	5×10^{12} to 5×10^{15} scaled	FV 0.23×0.31, 768×1152
FV	0.9×2.5	96×144		
FV	0.23×0.31	768×1152		

the transition to the $k^{-5/3}$ mesoscale regime, is obtained by scaling μ as $dx^{3.22}$, where dx is grid spacing. This empirical scaling law leads to μ decreasing by approximately a factor of 10 when the grid spacing is halved. Thus, for this study the value of μ is tuned using the quasi-uniform, 60-km simulation. The value of μ at other grid resolutions is then scaled following Boville (1991) and Takahashi et al. (2006).

c. Available potential energy design

Table 1 lists the aquaplanet simulations that we have performed. The simulations are configured following (Neale and Hoskins 2000a), with the "control" SST distribution as follows:

$$T_s(\lambda, \phi) = \begin{cases} 27\left[1 - \sin^2\left(\frac{3\phi}{2}\right)\right] & \text{if} \quad -\frac{\pi}{3} < \phi < \frac{\pi}{3}, \\ 0, & \text{otherwise}. \end{cases} \tag{1}$$

Each simulation is run for 5 years, with the first 6 months discarded for spinup, leaving 4.5 years for analysis. As stated previously, in each experiment with CAM-MPAS, the physical parameterizations, parameters, physics time step, and dynamics time step are unchanged. The one exception is the hyperdiffusion, which is scaled such that it decreases by a factor of 10 when the grid spacing is decreased by a factor of 2. The set of QUR simulations isolate the effects of horizontal resolution, whereas the VR simulation is used to evaluate the CAM-MPAS's potential for regional climate simulation. To provide context for this analysis, the new CAM-MPAS model is compared to CAM using the default finite-volume dynamical core (CAM-FV). Data saved from all simulations include standard monthly averaged output, as well as daily and 6-hourly (4× daily) fields for analysis of extreme events. All CAM-MPAS output data are remapped using conservative remapping (Jones 1999) to the nearest CAM-FV latitude–longitude grid in order to facilitate analysis, as indicated in Table 1. Unless otherwise noted, temporal means of the 4.5-yr analysis period are presented.

3. Results: Simulations with quasi-uniform resolution

a. Kinetic energy spectra

To assess the quality of the spatial discretization along with the model filtering, we begin by examining the kinetic energy (KE) spectra (e.g., Boville 1991), which describe how the energy of atmospheric motions is distributed across a range of spatial scales (Nastrom and Gage 1985). From theory and observations we expect that the KE spectra should have a k^{-3} slope at small wavenumbers k (wavelengths of about 1000–3000 km), which is thought to represent the downscale cascade of enstrophy [although this has recently been questioned by O'Gorman and Schneider (2007)]. A shallower slope ($k^{-5/3}$) has been observed at the transition to the mesoscale (Nastrom and Gage 1985). A number of attempts have been made to interpret the $k^{-5/3}$ region of the spectrum but there is currently no consensus concerning its dynamics—see the brief summary in Skamarock (2011). The spectra are computed from instantaneous values of the zonal and meridional winds using vector spherical harmonic transform (Adams and Swarztrauber 1997) and averaged over levels 6–20 (from middle to upper troposphere, about 600 to 50 hPa). Figure 2 shows the KE spectra for the four QUR CAM-MPAS simulations at 240-km, 120-km, 60-km, and 30-km grid spacing at different time periods throughout the simulations. All simulations show the k^{-3} slope, and the spectra are stable through time. The transition to the mesoscale ($k^{-5/3}$) slope is visible in the 30-km simulation. The effective resolution of the model (i.e., the scales that can be resolved by the model) is about eight times the horizontal grid spacing in each simulation, and the spectra for all the simulations agree in their resolved regions. Below the effective resolution in each simulation the kinetic energy is damped and decays relative to the actual spectrum. Our configuration of the hyperviscosity (section 2c) is designed to produce this damping, consistent with the filtering philosophy given in Skamarock (2004).

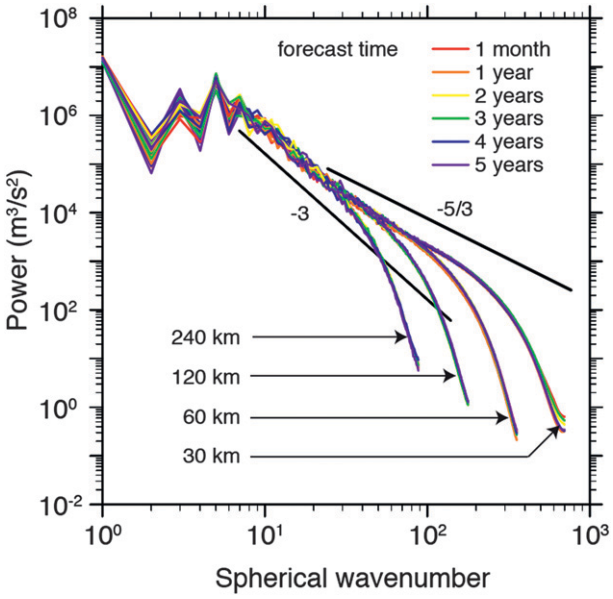

FIG. 2. Total kinetic energy spectra as a function of wavenumber after 1 month (red), and 1–5 years of simulation (orange–purple) for CAM-MPAS simulations at approximate grid spacings of 30 km, 60 km, 120 km, and 240 km.

b. General circulation

Although there is no one ''correct'' aquaplanet simulation, previous analyses of CAM aquaplanet experiments using different dynamical cores reveal consistent behavior, for example, Eulerian spectral core (Williamson and Olson 2003; Williamson 2008b,a), Eulerian/semi-Lagrangian fluid solver (EULAG) (Abiodun et al. 2008a,b), spectral element core (Mishra et al. 2011), as do other studies of the effects of model horizontal resolution on the general circulation (e.g., Boville 1991; Duffy et al. 2003; Iorio et al. 2004). As an initial examination of the CAM-MPAS coupling, we compare zonal means from the CAM-MPAS QUR simulations with the CAM-FV simulations. Although aquaplanet experiments are designed to be symmetric about the equator, differences between hemispheres can arise simply due to sampling error (Lorant and Royer 2001; Williamson 2008a).

Figure 3 shows a vertical cross section of the zonally averaged zonal wind (shaded) and vertical velocity (contours) for the four CAM-MPAS simulations, and the differences between CAM-MPAS (60 km) and CAM-FV at 0.5°, and CAM-MPAS (240 km) and CAM-FV at 2°. The contours of vertical velocity show a single peak over the equator in all simulations except in the CAM-MPAS 30-km and 60-km simulations, where a double peak straddling the equator is indicated, and all show subsidence over the subtropics. The magnitude of the mean upward vertical velocities is greater in both CAM-FV simulations than in the CAM-MPAS simulations at any resolution (Table 2, minimum zonally averaged omega). Even the 2° CAM-FV simulation has greater vertical velocities than CAM-MPAS (30 km), although the double peak is likely responsible.

The strength of the Hadley circulation can be measured by the maximum of the mean meridional streamfunction (Oort and Yienger 1996; Mitas and Clement 2005), which is listed in Table 2 for each simulation. As implied by the plots of vertical velocities, and the weaker meridional winds near the equator (Fig. 4), the Hadley circulation is stronger in the CAM-FV simulations than in the CAM-MPAS simulations at similar horizontal resolutions. The differences in Hadley circulation index between the CAM-MPAS and CAM-FV simulations listed in Table 2 are greater than the differences between hemispheres, implying that they are not simply the result of sampling error. Furthermore, the Hadley circulation strengthens with increasing resolution in the CAM-MPAS simulations as indicated in the Hadley strength index (Table 2), and by the minimum values of omega (-0.137 Pa s^{-1} at 30 km, -0.096 Pa s^{-1} at 240 km). These resolution differences appear to be robust as the 30-km and 240-km simulation values are separated by more than three standard deviations.

Considering the zonally averaged zonal wind (Fig. 3), in all simulations low-level tropical easterlies are found equatorward of 30°N/S, with a maximum near 10°N/S. A westerly jet with a single core is present at ~200 hPa, 30°N/S in all simulations, similar to that reported by Neale and Hoskins (2000b), although it is perhaps slightly lower in intensity in our simulations. Stronger tropical easterlies and midlatitude westerlies are notable in the CAM-FV 2° simulation (Table 2), whereas circulation differences in the CAM-MPAS 60 km and CAM-FV simulations are smaller and not consistently indicative of stronger winds in the FV simulation (not shown). The near-surface easterlies display increasing velocities with resolution in the CAM-MPAS simulations: the CAM-MPAS the 30-km maximum monthly average easterly wind speed at 925 hPa is -11.03 m s^{-1}, while at 240 km it is -9.35 m s^{-1}. In agreement with Williamson (2008a), the strength of the westerly jet decreases with increasing resolution, with a maximum value of 60.34 m s^{-1} in the 240-km CAM-MPAS simulations and 54.69 m s^{-1} in the 30-km simulation. Similarly, for the CAM-FV experiments, the jet has a maximum of 61.99 m s^{-1} at 2° and 58.05 m s^{-1} at 0.5°. The overall increase in the strength of the Hadley circulation with resolution decreases the meridional temperature gradient, resulting in the diminished strength of the westerly jet via thermal wind balance. However, at lower levels the strength of the westerlies increases with increasing

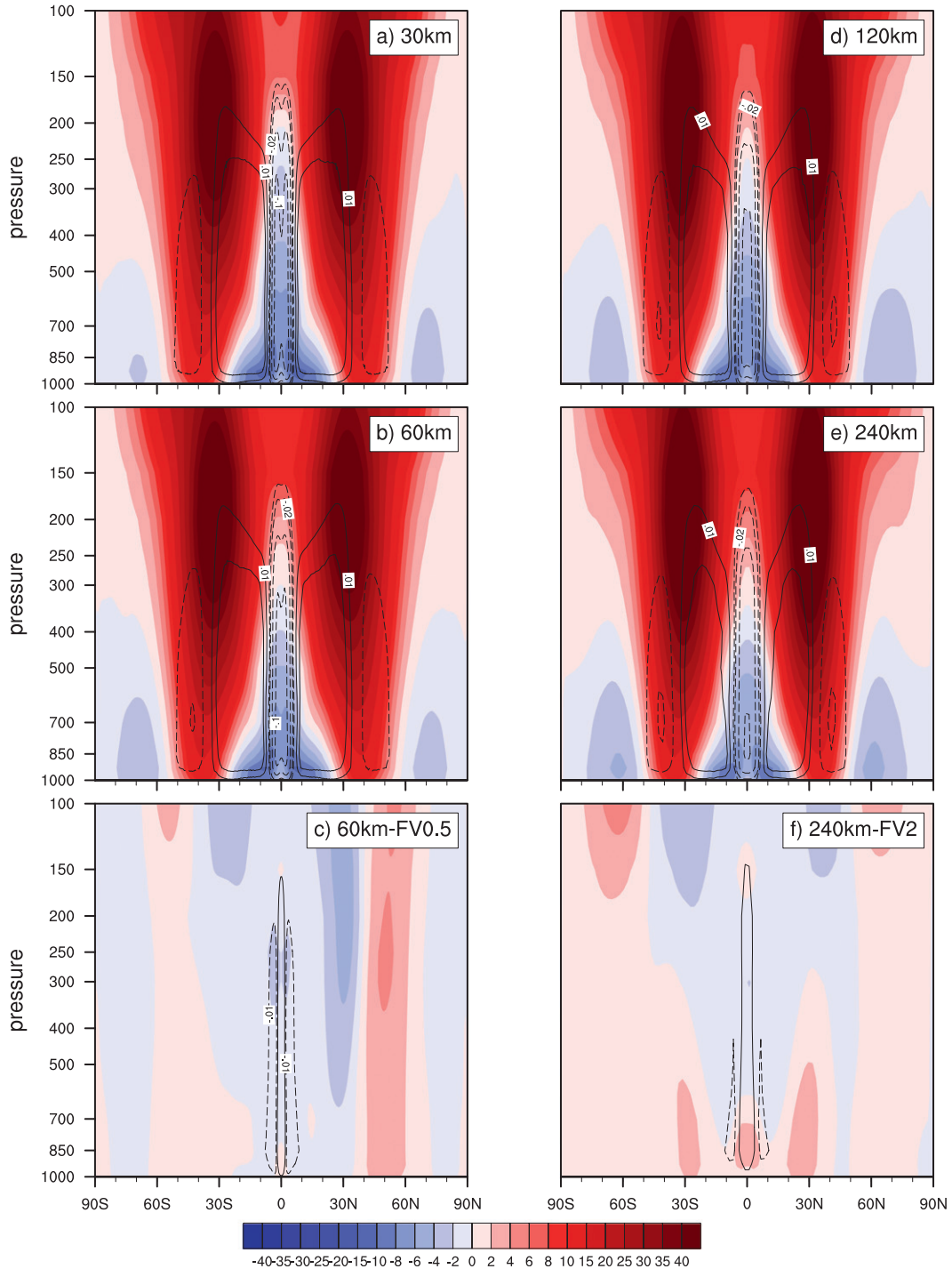

FIG. 3. Vertical cross section of zonally averaged zonal wind (m s^{-1}, shaded) and vertical velocity (Pa s^{-1}) for CAM-MPAS simulations at approximate grid spacings of (a) 30 km, (b) 60 km, (d) 120 km, and (e) 240 km, and CAM-MPAS–FV differences: (c) CAM-MPAS (60 km) minus CAM-FV at 0.47 × 0.63 and (f) CAM-MPAS (240 km) minus CAM-FV 1.9 × 2.5. Contours for omega are ±0.01, 0.02, 0.05, 0.10, and 0.15 for full fields and ±0.01 for differences. Negative contours are dashed.

TABLE 2. Select model quantities of monthly average fields.

Variable	MPAS 240	MPAS 120	MPAS 60	MPAS 30	FV2	FV0.5
Mean global precipitation (mm day^{-1})	2.93 (0.04)	3.04 (0.04)	3.10 (0.04)	3.19 (0.04)	2.86 (0.05)	3.07 (0.04)
Mean global convective precipitation (mm day^{-1})	1.40 (0.02)	1.23 (0.02)	1.06 (0.02)	0.90 (0.02)	1.56 (0.02)	1.13 (0.02)
Mean tropical precipitation (10°S–10°N) (mm day^{-1})	7.99 (0.34)	8.10 (0.30)	8.75 (0.39)	9.07 (0.30)	8.94 (0.52)	9.05 (0.40)
Mean tropical convective precipitation (10°S–10°N) (mm day^{-1})	5.18 (0.15)	4.43 (0.10)	4.12 (0.10)	3.65 (0.09)	6.18 (0.20)	4.29 (0.10)
Hadley strength index (global) (kg s^{-1}, divided by 110×10^{11})	2.25 (0.16)	2.53 (0.15)	2.63 (0.20)	2.85 (0.16)	2.65 (0.25)	2.73 (0.19)
Max zonal avg 200-hPa zonal wind (global) (m s^{-1})	60.34 (2.29)	59.04 (2.17)	55.37 (3.39)	54.69 (3.17)	61.99 (2.69)	58.05 (2.38)
Min zonal avg 925-hPa zonal wind (m s^{-1}) (20°S–20°N)	−9.35 (0.60)	−10.35 (0.46)	−10.57 (0.48)	−11.03 (0.38)	−10.66 (0.58)	−9.93 (0.51)
Min zonal avg 500-hPa omega (Pa s^{-1}) (10°S–10°N)	−0.10 (0.01)	−0.12 (0.01)	−0.13 (0.01)	−0.14 (0.01)	−0.13 (0.02)	−0.18 (0.02)

resolution poleward of 40°N/S, as implied by the zonal means of surface pressure (Fig. 5). In addition, the westerly maxima shift slightly poleward as resolution increases.

The net effect of these circulation features can be seen in the zonally averaged surface pressure (Fig. 5). Polar regions show lower surface pressure at higher resolution, indicating a mass transfer from polar to equatorial regions, which Williamson (2008a) attributed to ''increasing poleward transport of angular momentum with resolution, driving both stronger mid-latitude westerly winds and easterly trade winds'' in previous aquaplanet simulations using CAM. It is interesting to note that the CAM-MPAS simulations appear to behave more like higher-resolution simulations, as the CAM-MPAS 240-km and 60-km simulations show lower surface pressure at high latitudes than do their CAM-FV counterparts at 2° and 0.5°, respectively. Cloud fraction shows a strong resolution signal with cloud fraction decreasing at all latitudes with resolution, an effect that appears to intensify slightly (particularly in mid to high latitudes and the subtropics) as resolution increases. Zonal mean cross sections of specific humidity (Fig. 4, contours) indicate that the CAM-FV simulations are moister in the tropics (10°S–10°N) than are the CAM-MPAS simulations, and that moisture extends higher into the atmosphere. However, moisture increases with increasing resolution in the CAM-MPAS simulations. These key resolution effects observed in the CAM-MPAS QUR simulations, including a stronger Hadley circulation and more tropical moisture, have important implications for the variable resolution simulation discussed in section 4.

c. Precipitation

Maps of an instantaneous snapshot of precipitation rate for the QUR CAM-MPAS and CAM-FV simulations are shown in Fig. 6, and zonal mean precipitation rates are shown in Fig. 7. All simulations place the highest precipitation at or around the equator (the ITCZ), secondary maxima in the midlatitudes around 40°N/S (representing the effects of midlatitude baroclinic waves, evident in Fig. 6), and minima in the subtropics and polar regions. Global mean precipitation is near 3 mm day^{-1} in all simulations with higher amounts over the deep tropics (10°S–10°N) (7.99–9.07 mm day^{-1}) (Table 2). While the CAM-MPAS simulations have larger mean global precipitation rates than do their CAM-FV counterparts at similar resolutions, precipitation rates are lower over the tropics in CAM-MPAS, as indicated in Table 2, and the zonally averaged precipitation (Fig. 7). For example, in the 0.5° CAM-FV simulation zonal mean precipitation rates reach a maximum of 27 mm day^{-1} at the equator while the 60-km MPAS simulation is closer to 18 mm day^{-1} (Fig. 7). Further, the CAM-MPAS simulations show either a wider (120, 240 km) or double ITCZ (30, 60 km) compared to CAM-FV. Although double ITCZs are a common feature in aquaplanet simulations using CAM (e.g., Williamson and Olson 2003; Abiodun et al. 2008a,b; Williamson 2008a), an additional experiment (results not shown) indicates that the ITCZ simulation by CAM-MPAS is sensitive to the choice of the hyperdiffusion coefficient. In an experiment using the QUR 60-km mesh, reducing the coefficient results in a single ITCZ and increases precipitation rates over the equator.

As implied by the circulation analysis (i.e., increasing strength with resolution), precipitation increases with increasing resolution in the CAM-MPAS and CAM-FV simulations, particularly in the ITCZ (Table 2). This tendency for higher precipitation rates at higher resolution has been noted in other aquaplanet simulations (Lorant and Royer 2001; Williamson 2008b,a), as well as

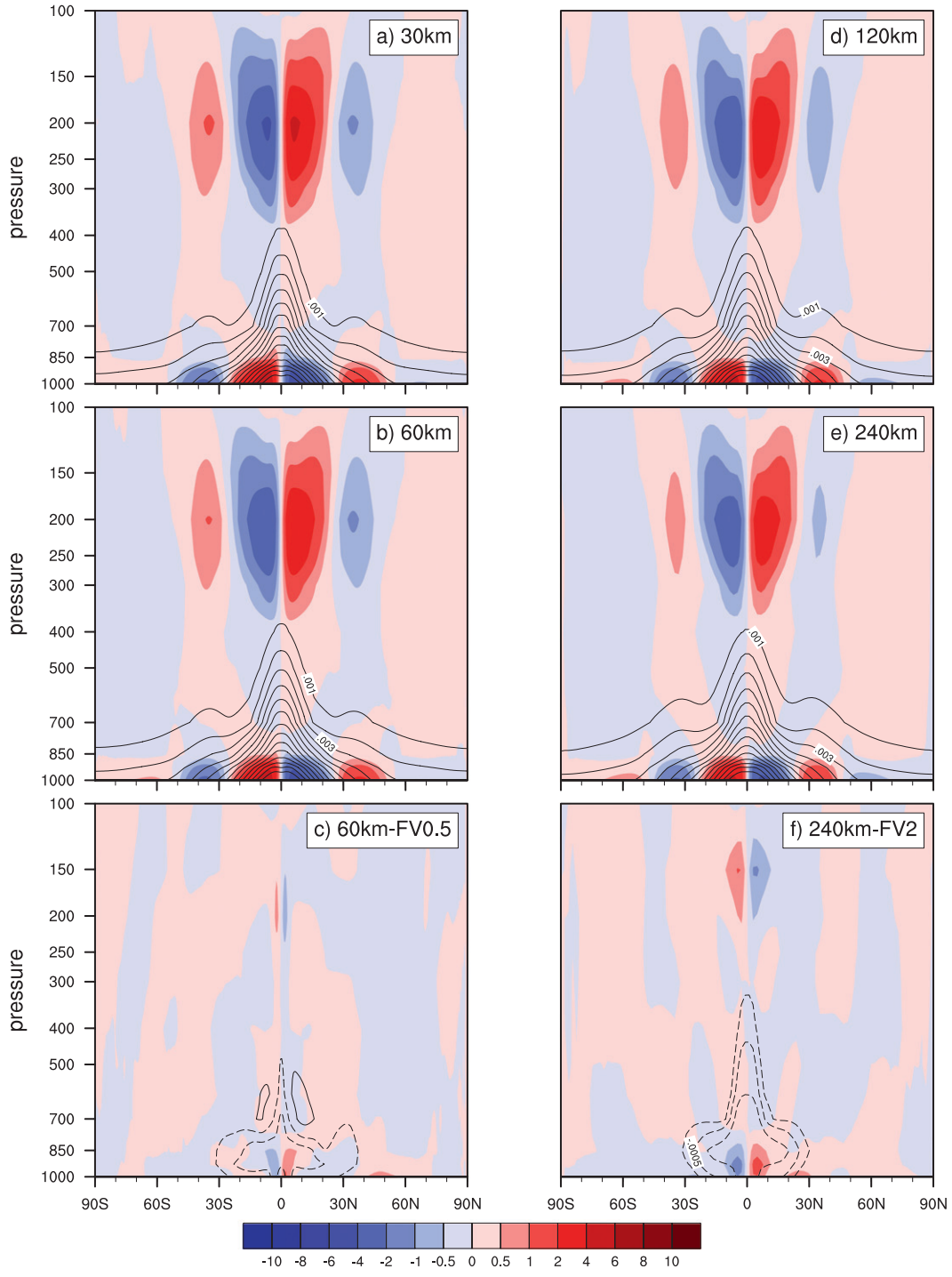

FIG. 4. Vertical cross section of zonally averaged meridional wind (m s^{-1}, shaded) and specific humidity (kg kg^{-1}) for CAM-MPAS simulations at approximate grid spacings of (a) 30 km, (b) 60 km, (d) 120 km, and (e) 240 km and CAM-MPAS–FV differences: (c) CAM-MPAS (60 km) minus CAM-FV at 0.47 × 0.63 and (f) CAM-MPAS (240 km) minus CAM-FV 1.9 × 2.5. Contours for specific humidity are by 0.001 for full field and ±0.0002, 0.0005, 0.001, 0.002, 0.004, and 0.008 for differences. Negative contours are dashed.

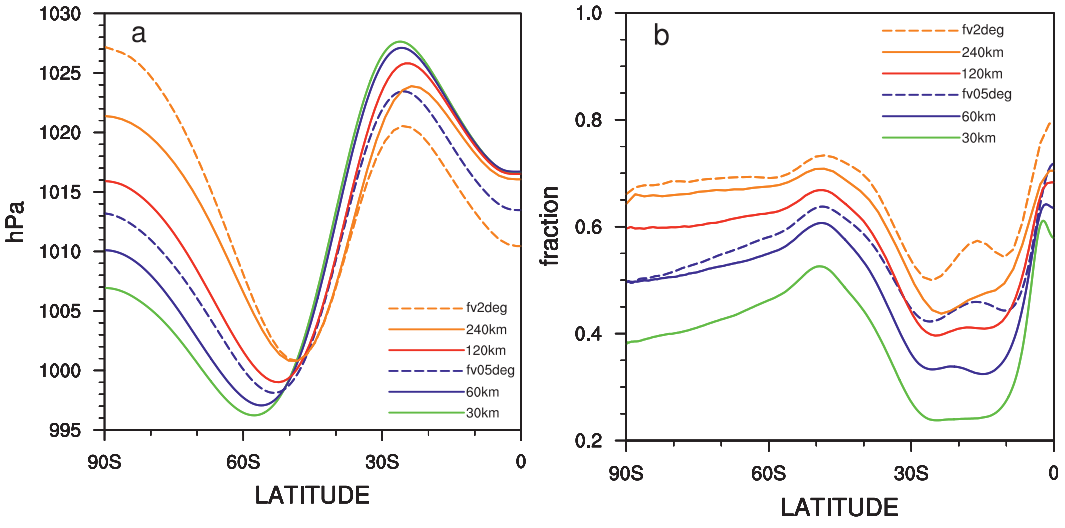

FIG. 5. Zonally averaged (a) surface pressure (hPa, PS) and (b) cloud fraction (fraction, CLDTOT) for CAM-MPAS simulations at approximate grid spacings of 30 (solid green), 60 (solid blue), 120 (solid red), and 240 km (solid orange) and for CAM-FV at 0.47 × 0.63 (dashed blue) and 1.9 × 2.5 (dashed orange). Hemispheres are averaged.

in global and regional "real world" simulations, even in midlatitudes (e.g., Duffy et al. 2003; Leung and Qian 2003; Iorio et al. 2004; Rauscher et al. 2010). Moreover, as resolution increases, the ratio of the convective precipitation to the large-scale precipitation decreases since average rates of convective precipitation decrease while total precipitation rates increase (Table 2). In other words, the increase in precipitation with higher resolution is due to increases in large-scale (or resolved) precipitation. This is an expected response to increasing model resolution, with the microphysics likely responding to enhanced grid-scale vertical velocities (e.g., Iorio et al. 2004; Boyle and Klein 2010; Li et al. 2011).

The precipitation probability density functions (PDFs) for lower intensity events (0–150 mm day^{-1}, 1 mm day^{-1} bins) and higher intensity events (0–1200 mm day^{-1}, 10 mm day^{-1} bins) over 10°S to 10°N are shown in Fig. 8. Overall, the CAM-MPAS 30-km model indicates similar frequencies of lower intensity events in the tropics as the other CAM-MPAS simulations at lower resolutions, but slightly higher frequencies of more intense events, which accounts for the higher precipitation overall. These resolution relationships hold even when the CAM-MPAS QUR 30-km simulation is regridded to the coarser 2° mesh. Both CAM-MPAS at 240 km and CAM-FV at 2° show higher frequencies of lower intensity events (0–50 mm day^{-1}), but a transition occurs at around 50 mm day^{-1}, where the CAM-MPAS 240km and CAM-FV at 2° begin to simulate lower intensities than the other models and resolutions. Also notable is the 0.5° CAM-FV simulation, which shows the highest frequency of very extreme events, greater than even the 30-km CAM-MPAS simulation. Again, this increased frequency of extreme precipitation events in the 0.5 CAM-FV simulation helps to account for the overall higher mean precipitation rates in that simulation. As with the circulation-resolution effects discussed in section 3b, the tendency for higher precipitation rates at higher resolutions in equatorial regions has a strong impact on our VR simulation, as will be seen in section 4.

CONVECTIVELY COUPLED EQUATORIAL WAVES

We examine the preferred temporal and spatial scales of convectively coupled equatorial waves using the methodology of Wheeler and Kiladis (1999). Six-hourly data are separated into equatorially symmetric and antisymmetric components over the first 1000 days of the 4.5-yr analysis period. Spectra are calculated for overlapping 96-day segments and then averaged over 10°S–10°N. Lines of equivalent depths h of 12, 25, and 50 m, related to the Kelvin wave phase speed via $c = \sqrt{gH}$ where g is the gravitational constant and H is the equivalent depth, are plotted. Westward propagating waves appear on the left-hand side of the diagram, whereas eastward propagating waves appear on the right-hand side. In the lower right-hand side of the normalized diagrams of the symmetric component of the outgoing longwave radiation (OLR), the diagonal lines from left to right indicate eastward propagating Kelvin waves, while westward propagating equatorial Rossby waves are shown on the left-hand side. Toward the top of the diagram, inertio–gravity waves are shown.

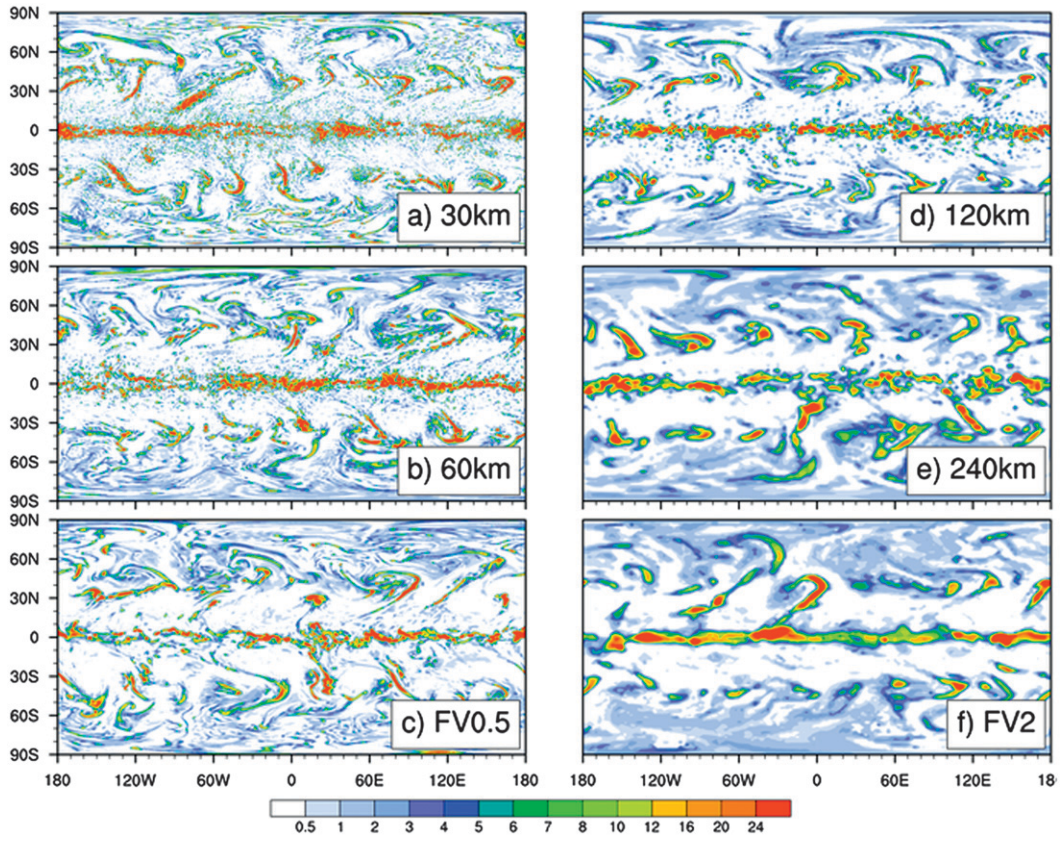

FIG. 6. Instantaneous snapshot of precipitation rate (mm day^{-1}) for CAM-MPAS simulations at approximate grid spacings of (a) 30 km, (b) 60 km, (d) 120 km, and (e) 240 km and CAM-FV at (c) 0.47 × 0.63 and (f) 1.9 × 2.5.

Figures 9 and 10 show the symmetric component of the normalized power spectra of OLR for the CAM-MPAS and CAM-FV simulations. Both CAM-MPAS and CAM-FV simulate eastward propagating Kelvin waves. Activity in the westward equatorial Rossby wave (ER, $n = 1$) and inertio–gravity portions of the spectrum appears to be weaker, although the CAM-MPAS simulations do show stronger ER activity compared to CAM-FV around zonal wavenumber 5 on the left side of the diagram. This is more apparent in the raw power spectra for the 60-km CAM-MPAS versus the 0.5° CAM-FV (not shown). The CAM-FV simulations show the most activity in the Kelvin portion of the spectrum centered at wavenumbers of 5 or less, whereas the CAM-MPAS simulations have more power at higher wavenumbers, in agreement with observations (Wheeler and Kiladis 1999, their Fig. 3b). (Although we are in the simplified setting of aquaplanet, we expect waves to propagate at similar speeds to those observed, just as we expect the kinetic energy spectra to share basic characteristics with observations.) However, the Kelvin phase speeds in CAM-MPAS are slower than in CAM-FV and observations. For example, the CAM-MPAS 60-km simulation has an equivalent depth of 12.5 m at around zonal wavenumber 5 (eastward Kelvin) whereas CAM-FV is centered at 25 m. All simulations indicate an increase in Kelvin phase speed with increasing wavenumber, which is opposite of what occurs in observations (Wheeler and Kiladis 1999). This same characteristic is found in CAM-SE and CAM-EUL and may therefore be attributable to the CAM physics (Mishra et al. 2011).

Also apparent in both sets of simulations is the increase in Kelvin wave phase speed with resolution. At 2°, CAM-FV has most of its Kelvin wave activity centered on lower wavenumbers at equivalent depths of about 12.5 m. At higher resolution (CAM-FV 0.5) this increases to 25 m. Of the CAM-MPAS simulations, the CAM-MPAS 30-km simulation agrees best with observations as the equivalent depth ranges from 50 at wavenumber 2 to between 25 and 50 around wavenumber 4. The raw spectra confirm the overall increase in power with resolution (not shown), similar to results from Williamson (2008a) using CAM3 and the Eulerian spectral dynamical core. Neither the CAM-MPAS nor the CAM-FV simulations indicate the presence of mixed

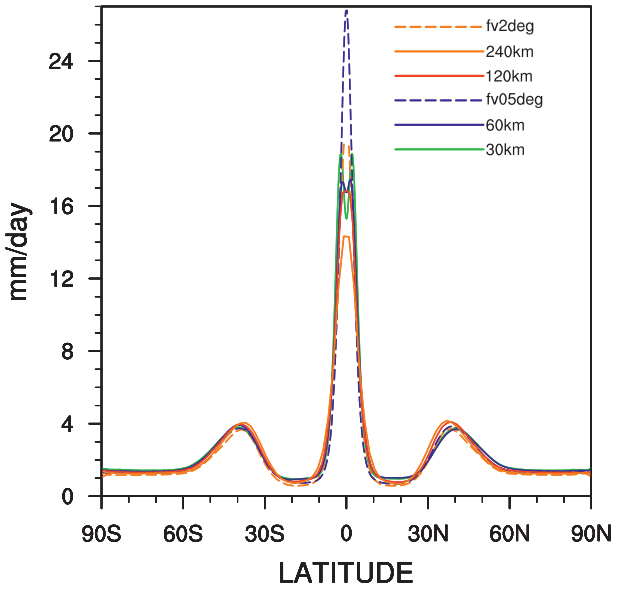

FIG. 7. Zonally averaged precipitation rate (mm day^{-1}) for CAM-MPAS simulations at approximate grid spacings of 30 (solid green), 60 (solid blue), 120 (solid red), and 240 km (solid orange) and for CAM-FV at 0.47 × 0.63 (dashed blue) and 1.9 × 2.5 (dashed orange).

Rossby–gravity waves (not shown) (e.g., Wheeler and Kiladis 1999, Fig. 3a).

4. Results: Variable resolution simulation

Since part of the motivation behind integrating the MPAS dynamical core into CAM and the full CESM system is to take advantage of its variable resolution capabilities for regional climate simulation, we also show results from a variable resolution (VR) aquaplanet simulation. This simulation allows us to explore the value of the high-resolution region in terms of its similarity to the global quasi-uniform 30-km simulation. Moreover, we can assess upscale effects from the high-resolution region to the coarse outer region since the absence of two-way interactions in one-way nesting approaches is an often-cited drawback to standard limited-area regional climate models (Giorgi and Mearns 1999; Laprise et al. 2008). Here we loosely define "upscale effects" as any differences between the coarse-resolution region in the VR simulation and the QU 240-km simulation. In section 3, we show that, as resolution increases in the CAM-MPAS QUR simulations, the general circulation strengthens (e.g., expansion and strengthening of the Hadley circulation) and precipitation rates increase globally and within the ITCZ. These resolution dependencies have important consequences for the variable resolution simulation, as we examine how the physical parameterizations react as the fluid enters and exits the high-resolution region.

a. Kinetic energy spectrum

The first question we ask is the following: are the fluid dynamics in the high-resolution region of the VR simulation similar to the fluid dynamics in the QUR 30-km simulation? Since our primary interest is the high-resolution region, the first task is to mask the entire low-resolution region. Since the variable resolution meshes

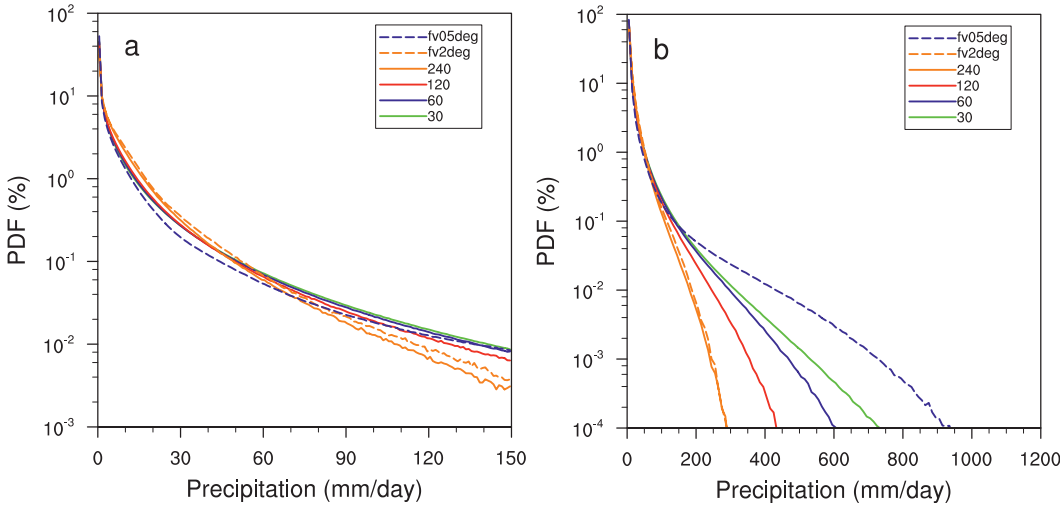

FIG. 8. Tropical (10°S–10°N) precipitation PDFs of (a) 0–150 mm day^{-1}, 1 mm day^{-1} bins, and (b) 0–1200 mm day^{-1}, 10 mm day^{-1} bins, for CAM-MPAS simulations at approximate grid spacings of 30 (solid green), 60 (solid blue), 120 (solid red), and 240 km (solid orange) and for CAM-FV at 0.47 × 0.63 (dashed blue) and 1.9 × 2.5 (dashed orange). Six-hourly (4× daily) instantaneous data are used.

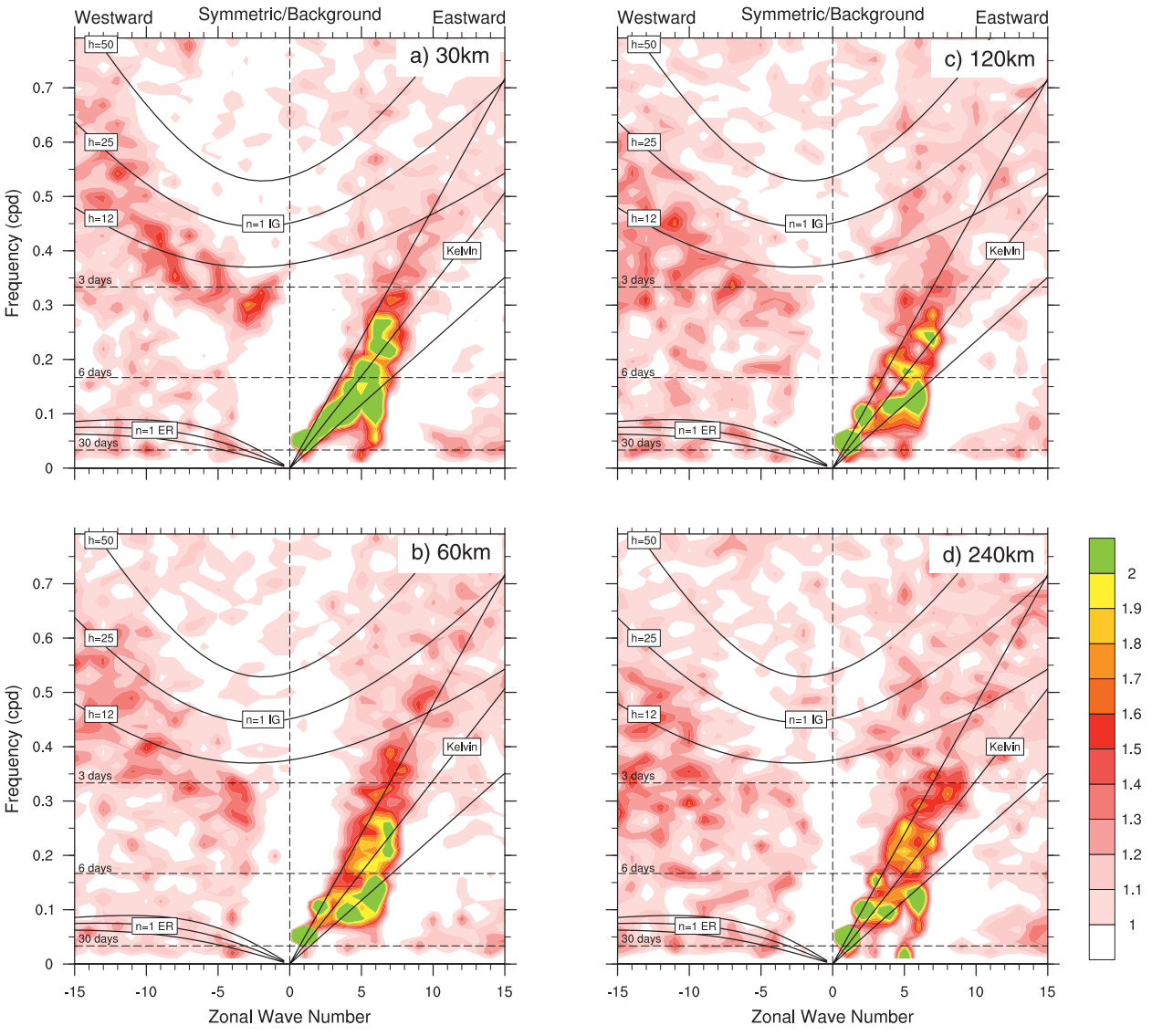

FIG. 9. Wavenumber–frequency diagrams of outgoing longwave radiation (W m^{-2}) from 10°S to 10°N. Symmetric component of normalized power spectra is shown, similar to Fig. 3 of Wheeler and Kiladis (1999) for quasi-uniform CAM-MPAS simulations at approximate grid spacings of (a) 30 (b) 60, (c) 120, and (d) 240 km. Six-hourly (4× daily) instantaneous data are used over the first 1000 days of the simulations.

are created with a single scalar density function that varies from one in the high-resolution region to near zero in the low-resolution region, the mesh density function provides an excellent filter to mask out the low-resolution region in the VR simulation. First, the zonal and meridional components of the wind field are multiplied by the mesh density function so that we retain the kinetic energy over only a portion of the global domain. It is important to note that we apply this filtering approach to *both* the VR and QUR kinetic energy fields. We then compute the kinetic energy spectrum by computing the spherical harmonics of the filtered VR and QUR kinetic energy fields. This approach corrupts wavelengths longer than the size of the high-resolution region, that is, at wavenumbers smaller than approximately 6. Our analysis indicates that shape of the spectrum for wavelengths substantially smaller than the high-resolution region is represented fairly with this filtering technique. The resulting kinetic energy power spectra for the VR and QUR simulations are shown in Fig. 11. The spectra are remarkably similar—both showing that the spectrum transitions from k^{-3} to $k^{-5/3}$ at approximately 400 km. The amplitude of the QUR power spectrum shown in Fig. 11 is about a factor of 10 smaller than that shown in

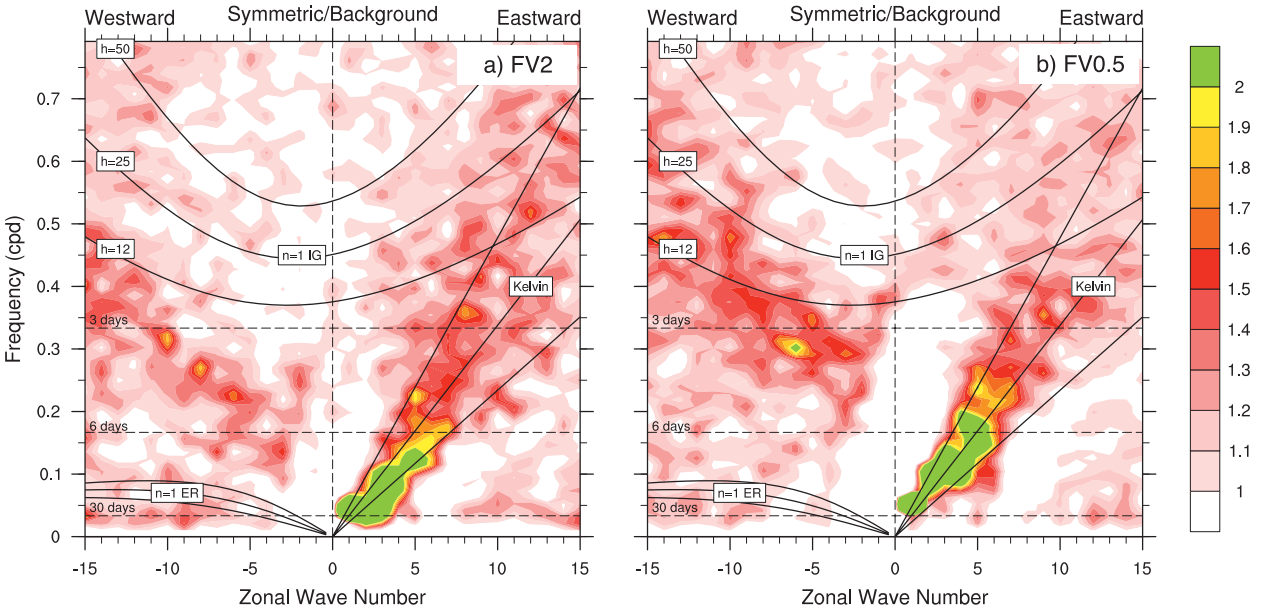

FIG. 10. Wavenumber–frequency diagrams of outgoing longwave radiation (W m^{-2}) from 10°S to 10°N. Symmetric component of normalized power spectra is shown, similar to Fig. 3 of Wheeler and Kiladis (1999) for FV simulations at (a) 1.9 × 2.5 and (b) 0.47 × 0.63. Six-hourly (4× daily) instantaneous data are used over the first 1000 days of the simulations.

Fig. 2 because only 10% of the global kinetic energy field is retained after filtering.

b. *Precipitation*

Figure 12 shows the zonally averaged precipitation for the CAM-MPAS VR simulation, the CAM-MPAS 240-km QUR simulation, and the CAM-MPAS 30-km QUR simulation. Precipitation in the VR simulation is also separated further into its high-resolution and low-resolution region. Comparing first with the QUR CAM-MPAS 240-km simulation, the full VR precipitation rates are similar, although slightly higher, and a faint double ITCZ is apparent that is absent in the CAM-MPAS 240-km simulation. In contrast to the CAM-MPAS 30-km QUR simulation, precipitation rates are lower; however, a double ITCZ is present and it is amplified when considering the high-resolution region alone (dashed green). Most interestingly, the high-resolution region appears to have an upscale effect as even the coarse-resolution region alone (dash-dotted orange) shows a slight double ITCZ.

Maps of average precipitation and vertically integrated precipitable water (TMQ) for the CAM-MPAS VR, 30-km, and 240-km simulations further illustrate the differences in tropical precipitation between the simulations (Fig. 13). Note that the coarse-resolution region in the VR simulation appears noisy and retains the hexagonal imprint of its native mesh due to the conservative remapping (Jones 1999) of the entire VR mesh to the high resolution FV 0.23 × 0.31 mesh. The overall greater tropical precipitation is evident in the CAM-MPAS 30-km simulation compared to both QUR CAM-MPAS 240-km and VR simulations. Of interest in the VR simulation is a maximum in precipitation on the western side of the high-resolution region near 30°W,

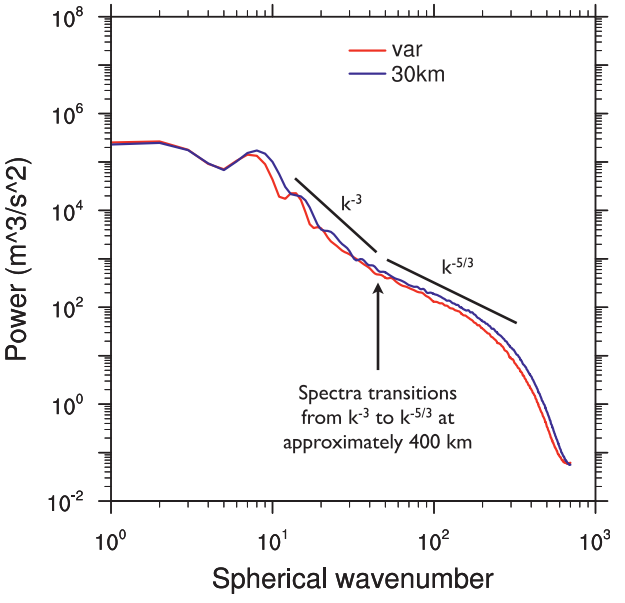

FIG. 11. Total kinetic energy spectra as a function of wavenumber for the high-resolution region in CAM-MPAS simulations at quasi-uniform high resolution (30 km, blue) and VR (red).

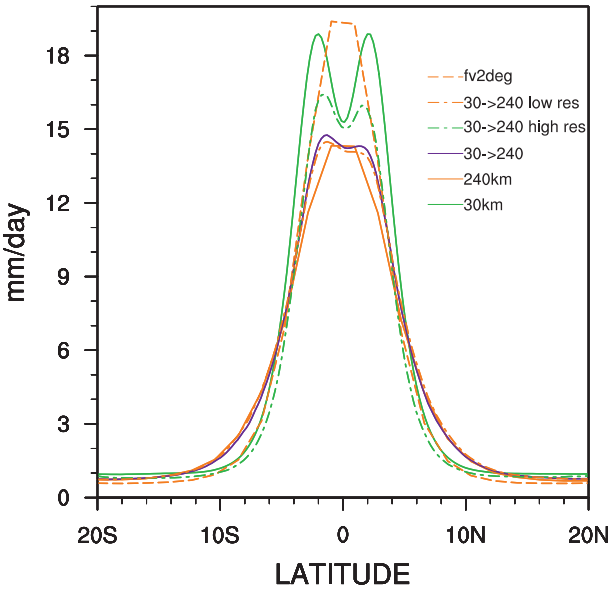

FIG. 12. Zonally averaged precipitation rate (mm day^{-1}) from 20°S to 20°N for CAM-MPAS simulations at approximate grid spacings of 30 km (solid green) and 240 km (solid orange) and with variable resolution (30 to 240 km) (purple). The high-resolution region of the variable-resolution simulation is depicted as dashed green, and the outer coarse-resolution region is in dashed orange. CAM-FV is at 1.9 × 2.5 (dashed orange).

corresponding to a similarly located maximum in vertically integrated precipitable water (Fig. 13). The CAM-MPAS 240-km simulation (equivalent to the coarse region of the variable resolution simulation) has lower vertically integrated precipitable water in equatorial regions, whereas the CAM-MPAS 30-km simulation appears to have a higher equilibrium state. The VR simulation therefore shows characteristics of both.

As discussed in section 3b, wind speeds and the Hadley circulation strength increase with increasing resolution in the QUR simulations. Here, similar effects occur in our fine- and coarse-resolution regions in the VR simulation. A cross section of specific humidity and zonal velocities from 0° eastward to 360° averaged from 5°S to 5°N for the VR simulation (not shown) indicates that wind speeds increase as the flow enters the high-resolution region from east to west. Moisture is transported westward across the high-resolution region, resulting in a local maximum in both moisture and precipitation at the western edge of the high-resolution region. The latter is illustrated by departures from the zonal mean precipitation in Fig. 14a (shaded). Associated with this precipitation anomaly is a diabatic heating anomaly at ~30°W in the VR simulation (not shown). This heating anomaly initiates a Gill-type response (Gill 1980), as indicated by the 200-hPa eddy velocity potential and eddy streamfunction (Figs. 14a,b). An upper-level anticyclone is found to the northwest of the positive heating anomaly. Negative velocity potential anomalies from the zonal mean indicate upper-level divergence around the western periphery of the high-resolution region and compensating upper-level convergence and subsidence to the east. The latter also appear to be the equivalent of a negative heating anomaly (30°–60°E), resulting in the complex pattern of streamfunction anomalies.

This precipitation maximum on the western side of the high-resolution region in the VR simulation and the associated anomalous circulations appear to be a response of the model's moist physics to the local mesh refinement. In fact, this zonally asymmetric response could have been inferred from the set of QUR simulations analyzed in section 3, where our results indicated a stronger Hadley circulation and higher tropical precipitation rates in the QUR 30-km simulation compared to the 240-km simulation. To confirm this conclusion, a Held–Suarez (Held and Suarez 1994) test was run for the variable resolution case for four years, slightly beyond the standard 1200-day simulation. In a Held–Suarez test, model physics are replaced by prescribed forcing and dissipation. The 200-hPa eddy velocity potential field from the last year of that experiment (Fig. 14c) does not show a similar response to the full-physics aquaplanet variable resolution (the same contour interval is used as in Fig. 14b). Furthermore, Held–Suarez tests performed for the QUR 30-km and 240-km meshes indicate little resolution dependency as well (not shown), highlighting the interaction between the moist physics and the variable resolution mesh in driving this anomalous circulation.

Longitude–time Hovmöller diagrams of precipitation and convective precipitation (Fig. 15) averaged from 10°S to 10°N further illustrate the effects of the mesh refinement and the response of the model physics in the CAM-MPAS 30-km, 240-km, and VR simulations. Since the analysis of convectively coupled equatorial waves showed active eastward propagating Kelvin wave activity, we filter the total and convective precipitation fields to diagnose Kelvin wave activity (black contours). The tendency for the convective parameterization to become less active with increasing resolution is evident in Figs. 15d–f when comparing the CAM-MPAS 30-km simulation (Fig. 15d) to the CAM-MPAS 240-km simulation (Fig. 15f). The variable resolution simulation combines the features of these two simulations, indicating a switch from a more active convective parameterization in the low-resolution region to a dominance of large-scale precipitation in the high-resolution region, which is marked by vertical lines. Nonetheless, waves do appear to propagate through the coarse-mesh region into the fine-mesh region and vice versa. While only qualitative in

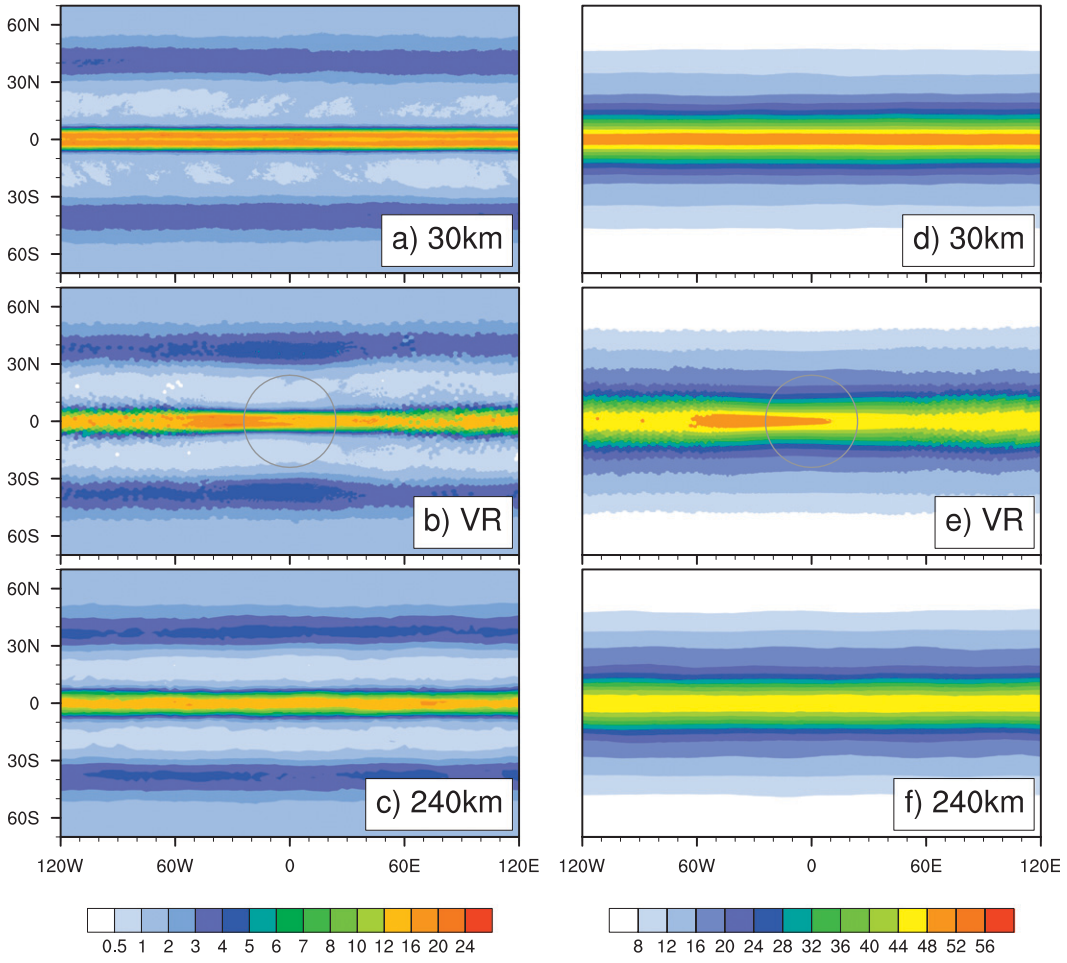

FIG. 13. (left) Precipitation rate (mm day^{-1}) and (right) total vertically integrated precipitable water (kg m^{-2}) for CAM-MPAS simulations (a),(d) at 30 km, (b),(e) with variable resolution, and (c),(f) at 240 km. Note that the coarse-resolution region in the VR simulation appears noisy and retains the hexagonal imprint of its native grid due to the conservative remapping of the entire VR mesh to the high-resolution FV 0.23 × 0.31 grid. The high-resolution region of the VR mesh is outlined in gray.

nature, Fig. 15 gives no indications of waves being spuriously reflected, refracted, or strongly damped in the vicinity of the mesh transition zone.

5. Discussion and conclusions

We have analyzed a series of simulations conducted with the new MPAS hydrostatic atmospheric dynamical core implemented within the Community Atmosphere Model (CAM). Simulations with quasi-uniform meshes indicate results similar to previous aquaplanet simulations with different dynamical cores in CAM: as resolution increases, the general circulation strengthens and precipitation rates increase globally and within the ITCZ. For example, Abiodun et al. (2008a) noted the same expansion and strengthening of the Hadley circulation, reduced peak strength of the westerlies, increased precipitation, and even the change from a single ITCZ to double ITCZ with increasing resolution in their simulations with CAM-EULAG. Deviations from the default FV dynamical core include a weaker overall general circulation that is more pronounced when comparing the 2° simulations, weaker tropical precipitation rates, and a double ITCZ that is manifested in the higher resolution CAM-MPAS simulations. The presence of a double ITCZ is sensitive not only to resolution but also to the coefficient of the ∇^4 dissipation, thus indicating an extremely sensitive relationship between the action of the moist physical parameterizations and the character of the fluid flow near the grid scale. Analysis of the precipitation PDF in the tropics suggests that extreme precipitation events are more frequent in the CAM-FV simulation, at least at the 0.5° resolution. A Wheeler–Kiladis (1999) spectral analysis shows most tropical activity in

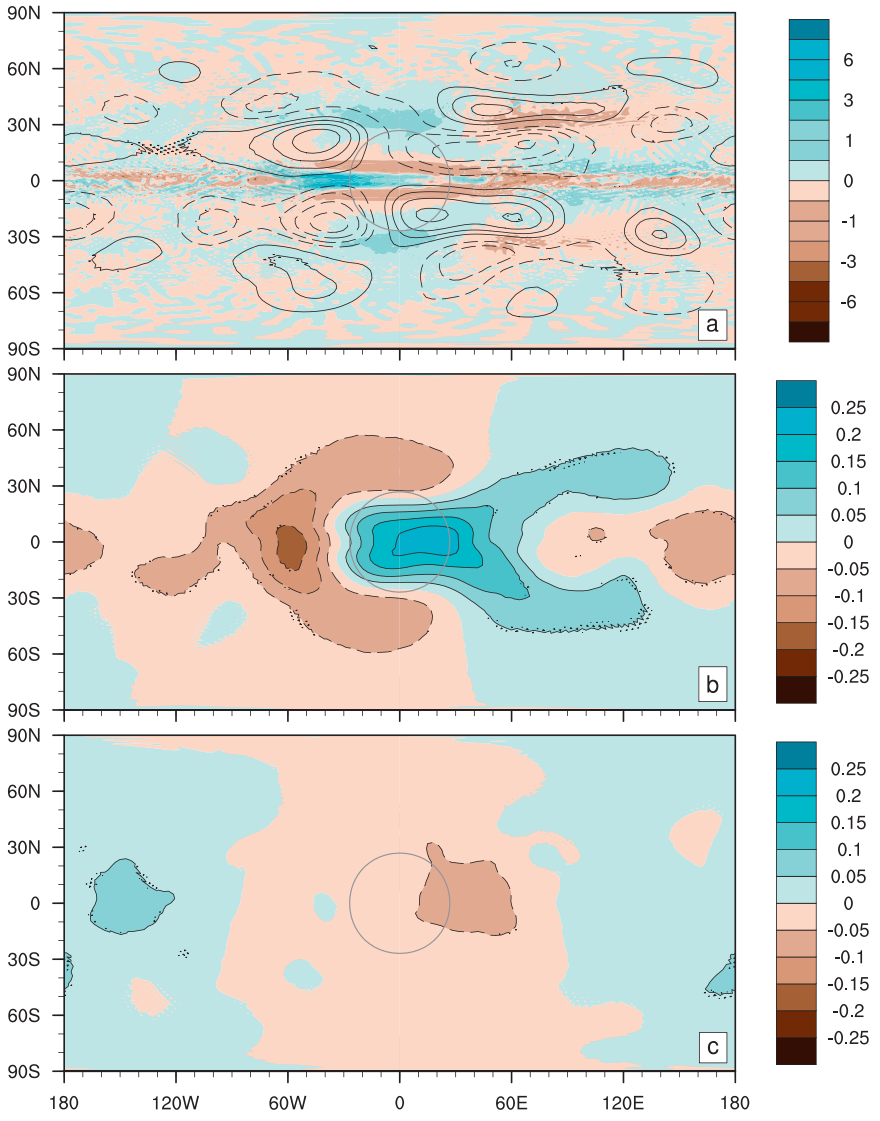

FIG. 14. (a) 200-hPa eddy streamfunction ($m^2\ s^{-1}$, divided by 10×10^6, contour) and precipitation deviations from the zonal mean (mm day^{-1}, shaded) for the CAM-MPAS variable resolution simulation and 200-hPa eddy velocity potential ($m^2\ s^{-1}$, divided by 10×10^6) for the (b) variable-resolution aquaplanet simulation and (c) Held–Suarez simulation. The high-resolution region of the VR mesh is outlined in gray.

the Kelvin portion of the spectrum, with little in the way of mixed Rossby–gravity waves. The CAM-MPAS simulations indicate slightly greater westward equatorial Rossby wave activity than do the CAM-FV simulations.

A variable resolution simulation performed with CAM-MPAS does show similarities between its high-resolution 30-km region and the quasi-uniform global 30-km simulation, particularly in the kinetic energy spectrum and in the presence of a double ITCZ that extends beyond the high-resolution region into the coarse-resolution region. The latter indicates an ''upscale'' effect from the high to the low resolution region. However, the interaction between the moist physics and the mesh refinement region produces a region of high precipitation and an associated diabatic heating anomaly on the western periphery and further downstream of the high-resolution region. This zonally asymmetric response affects the circulation over the entire tropics, although it is felt most acutely between about 90°W and 90°E, or three times the width of the high-resolution region. To confirm that the varying response of physical parameterizations with grid resolution is responsible for this zonally asymmetrical heating, we conducted Held and Suarez (1994) test case simulations where the

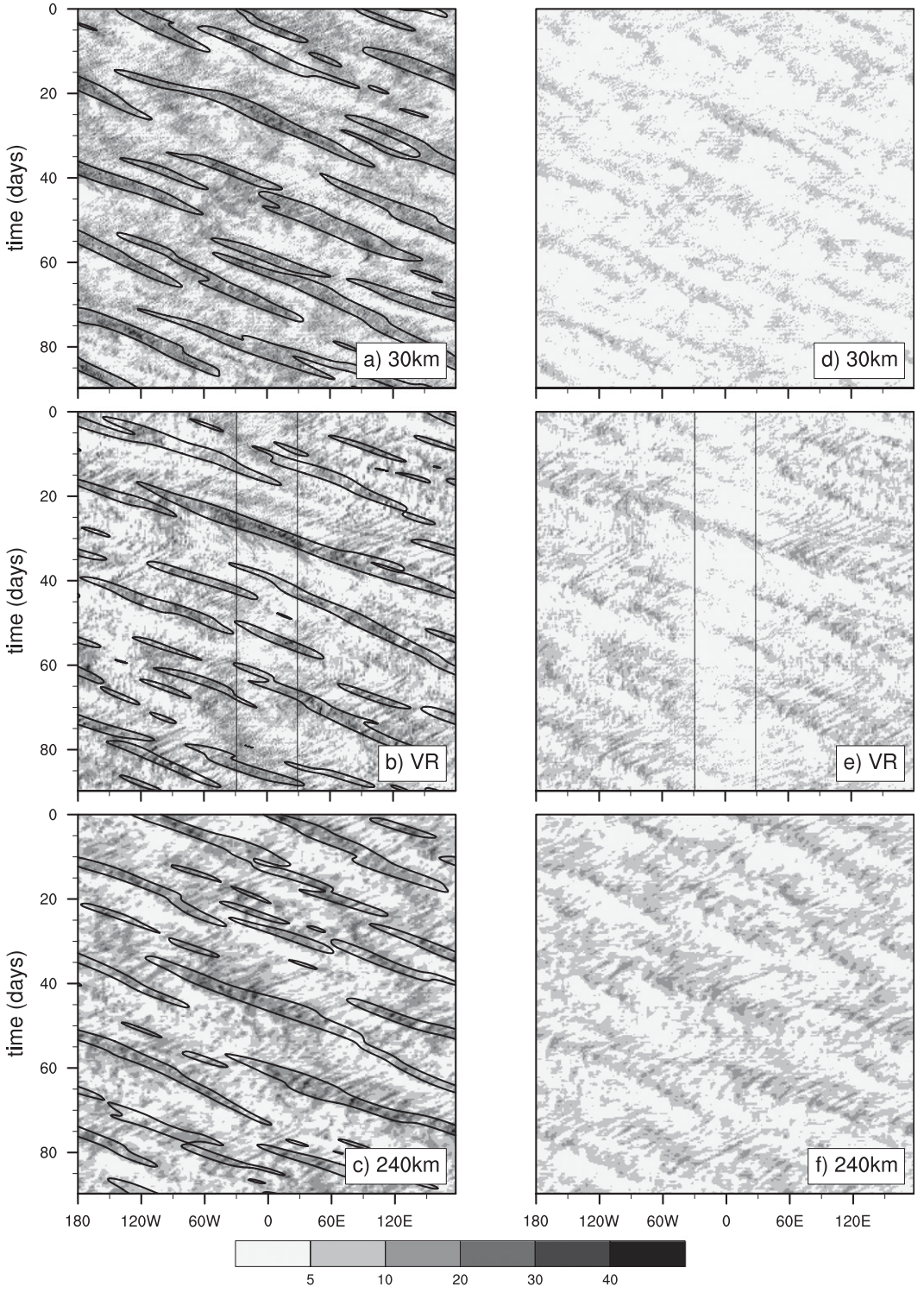

FIG. 15. Hovmöller (time–longitude) diagram of (left) precipitation (PRECT) (mm day^{-1}; shaded) and (right) convective precipitation (PRECC) (shaded) averaged from 10°S to 10°N over a 90-day period for (a),(d) CAM-MPAS (30 km), (b),(e) CAM-MPAS VR, and (c),(f) CAM-MPAS (240 km). Contours are data filtered to show Kelvin wave activity (2.5 mm day^{-1} contour interval). Four-times-daily data are used. The high-resolution region of the VR mesh is outlined in gray.

idealized ''physics'' should not be sensitive to grid resolution. In contrast to our aquaplanet results, the variable resolution mesh paired with the Held–Suarez forcing produces a nearly zonally symmetric response. Combined with previous results from shallow-water test cases using variable resolution meshes (Ringler et al. 2011), we conclude that differing response of the model's moist physics at different resolutions is the root cause of the zonally asymmetric diabatic heating. This resolution dependency of the physics is readily apparent in the QUR simulations.

These variable resolution simulation results highlight two key issues within regional climate simulation: 1) the choice of the high-resolution region (location and size) and 2) scale dependencies in model parameterizations. Focusing on the first, the response to the mesh refinement region is likely dependent on the difference in resolution between the high and low resolution region as well as on the size and location of the high-resolution region. For example, here the location of our high-resolution region on the equator likely introduces the greatest potential for such grid–physics interactions where precipitation rates are highest and resolution sensitivity is greatest, as demonstrated by the suite of QUR simulations. A variable resolution mesh should be tested in a midlatitude region to determine if similar order-of-magnitude effects occur. Similar ''domain dependency'' has been studied and documented extensively in traditional nested RCM studies (e.g., Jones et al. 1995; Seth and Giorgi 1998; Rauscher et al. 2006), which could help to inform the design of VR simulations.

Second, our results highlight the scale dependency of the model physical parameterizations. The underlying premise of a parameterization is that it mimics a process that is not directly simulated. Within this conceptual model, the sum of the directly simulated (resolved) and parameterized (unresolved) responses should not change with model grid scale. However, our results clearly indicate that the opposite is true. This is particularly apparent in the sensitivity of total precipitation and total precipitable water to model resolution. In the variable resolution simulation, the high-resolution region resembles the quasi-uniform global high-resolution simulation. However, the differing response of the moist physics in the mesh refinement region compared to the coarse-resolution domain results in an undesirable zonal asymmetry. This finding underscores the utility of the idealized test cases: in real-world simulations such responses could be inappropriately attributed to variations in the lower boundary condition (e.g., topography or land–sea contrasts) unless additional experiments are performed to separate these effects (e.g., Giorgi and Marinucci 1996; Gao et al. 2006). Most importantly, our results demonstrate once again that physical parameterizations are not entirely scale-aware. While tuning of physics parameters can compensate for this shortcoming in global, quasi-uniform simulations, variable-resolution simulations highlight this deficiency. For example, high-resolution global quasi-uniform simulations are pushing grid scales to a few tens of kilometers or less, where the scale separation assumptions underlying many cloud parameterization schemes lose their foundational support. Designing scale-aware parameterizations is clearly the next great modeling challenge.

Despite the response to the mesh refinement region, the results from our CAM-MPAS simulations are encouraging in that CAM-MPAS provides a reasonable aquaplanet simulation that is comparable to simulations using other dynamical cores implemented within CAM. Moreover, since the ''error'' incurred from using a variable resolution mesh can be measured by the amplitude of the zonally asymmetric response, improvements in model physical parameterizations can be tracked by measuring this error in future simulations. Therefore, future work will focus on evaluating the zonally asymmetric response when using CAM5 physics in place of CAM4 physics in aquaplanet simulations and testing CAM-MPAS in real-world AMIP-style simulations, with and without mesh refinement.

In the context of regional climate simulation, the global variable-resolution approach holds potential advantages over the traditional limited-area approach employed by RCMs. First, using a single dynamical core for both the low-resolution and high-resolution regions offers a level of consistency not typically found in simulations conducted with RCMs. Furthermore, since a variable resolution framework requires no lateral boundary conditions from GCMs, regional modelers are granted autonomy in performing their simulations. Traditionally regional modelers must wait until the GCM simulations are completed, often at different institutions, modify existing codes to use the data as initial and lateral boundary conditions, obtain the data, and run the simulations, resulting in considerable lag times between GCM data availability and RCM data availability. These various hurdles greatly hinder efforts to include up-to-date regional climate information in assessment reports and to provide regional climate data to end users. For example, multimodel results from downscaling efforts of the CMIP3 models [e.g., ENSEMBLES (Hewitt and Griggs 2004) and the North American Regional Climate Change Assessment Program (NARCCAP) (Mearns et al. 2009)] used in the Fourth Assessment Report of the Intergovernmental

Panel on Climate Change are now only beginning to become available for the Fifth Assessment Report. Finally, and most importantly, the approach that we have analyzed above allows for regional climate simulation to be conducted within the *exact* same modeling framework that is used for global climate system modeling. Thus, this approach provides the opportunity for the global climate modeling community and the regional climate modeling community to share a common modeling framework and to readily benefit from each other's progress.

Acknowledgments. We thank two anonymous reviewers for their comments that helped to improve the quality and presentation of this manuscript. This work is supported by the DOE 07SCPF152 for the ''Development of Frameworks for Robust Regional Climate Modeling.'' Work on the part of LLNL was performed under the auspices of the U.S. Department of Energy by Lawrence Livermore National Laboratory under Contract DE-AC52-07NA27344. The efforts of Dan Bergman and Jeff Painter in helping to couple MPAS with CESM are very much appreciated. SR thanks Adrian Tompkins for helpful comments.

REFERENCES

Abiodun, B. J., J. M. Prusa, and W. J. Gutowski, 2008a: Implementation of a non-hydrostatic, adaptive-grid dynamics core in CAM3. Part I: Comparison of dynamics cores in aquaplanet simulations. *Climate Dyn.,* **31,** 795–810.

——, W. J. Gutowski, and J. M. Prusa, 2008b: Implementation of a non-hydrostatic, adaptive-grid dynamics core in CAM3. Part II: Dynamical influences on ITCZ behavior and tropical precipitation. *Climate Dyn.,* **31,** 811–822.

Adams, J. C., and P. N. Swarztrauber, 1997: Spherepack 2.0: A model development facility. NCAR Tech. Note NCAR/TN-436-STR, 58 pp.

Boville, B. A., 1991: Sensitivity of simulated climate to model resolution. *J. Climate,* **4,** 469–486.

Boyle, J., and S. A. Klein, 2010: Impact of horizontal resolution on climate model forecasts of tropical precipitation and diabatic heating for the TWP-ICE period. *J. Geophys. Res.,* **115,** D23113, doi:10.1029/2010JD014262.

Déqué, M., and Coauthors, 2005: Global high resolution versus limited area model climate change projections over Europe: Quantifying confidence level from PRUDENCE results. *Climate Dyn.,* **25,** 653–670.

Dickinson, R. E., R. M. Errico, F. Giorgi, and G. Bates, 1989: A regional climate model for the western United States. *Climatic Change,* **15,** 383–422.

Du, Q., V. Faber, and M. Gunzburger, 1999: Centroidal Voronoi tessellations: Applications and algorithms. *SIAM Rev.,* **41,** 637–676.

Duffy, P. B., B. Govindasamy, J. P. Iorio, J. Milovich, K. R. Sperber, K. E. Taylor, M. F. Wehner, and S. L. Thompson, 2003: High-resolution simulations of global climate, Part 1: Present climate. *Climate Dyn.,* **21,** 371–390.

Fox-Rabinovitz, M., G. Stenchikov, M. Suarez, and L. Takacs, 1997: A finite-difference GCM dynamical core with a variable resolution stretched grid. *Mon. Wea. Rev.,* **125,** 2943–2968.

——, J. Côté, B. Dugas, M. Déqué, and J. McGregor, 2006: Variable resolution general circulation models: Stretched-grid model intercomparison project (SGMIP). *J. Geophys. Res.,* **111,** D16104, doi:10.1029/2005JD006520.

Gao, X., Y. Xu, Z. Zhao, J. S. Pal, and F. Giorgi, 2006: On the role of resolution and topography in the simulation of East Asia precipitation. *Theor. Appl. Climatol.,* **86,** 173–185.

Gettelman, A., H. Morrison, and S. J. Ghan, 2008: A new two-moment bulk stratiform cloud microphysics scheme in the Community Atmosphere Model, version 3 (CAM3). Part II: Single-column and global results. *J. Climate,* **21,** 3660–3679.

Gill, A. E., 1980: Some simple solutions for heat-induced tropical circulation. *Quart. J. Roy. Meteor. Soc.,* **106,** 447–462.

Giorgi, F., and L. O. Mearns, 1991: Approaches to the simulation of regional climate change: A review. *Rev. Geophys.,* **29,** 191–216.

——, and M. R. Marinucci, 1996: An investigation of the sensitivity of simulated precipitation to model resolution and its implications for climate studies. *Mon. Wea. Rev.,* **124,** 148–166.

——, and L. O. Mearns, 1999: Introduction to special section: Regional climate modeling revisited. *J. Geophys. Res.,* **104,** 6335–6352.

——, C. Jones, and G. Asrar, 2009: Addressing climate information needs at the regional level: The CORDEX framework. *WMO Bull.,* **58,** 175–183.

Held, I. M., and M. J. Suarez, 1994: A proposal for the intercomparison of the dynamical cores of atmospheric general circulation models. *Bull. Amer. Meteor. Soc.,* **75,** 1825–1830.

Hewitt, C. D., and D. J. Griggs, 2004: ENSEMBLES-based predictions of climate changes and their impacts. *Eos, Trans. Amer. Geophys. Union,* **85,** 566.

Iorio, J. P., P. B. Duffy, B. Govindasamy, S. L. Thompson, M. Khairoutdinov, and D. Randall, 2004: Effects of model resolution and subgrid-scale physics on the simulation of precipitation in the continental United States. *Climate Dyn.,* **23,** 243–258.

Jones, P. W., 1999: First- and second-order conservative remapping schemes for grids in spherical coordinates. *Mon. Wea. Rev.,* **127,** 2204–2210.

Jones, R. G., J. M. Murphy, and M. Noguer, 1995: Simulation of climate change over Europe using a nested regional-climate model. I: Assessment of control climate, including sensitivity to location of lateral boundaries. *Quart. J. Roy. Meteor. Soc.,* **121,** 1413–1449.

Ju, L., T. Ringler, and M. Gunzburger, 2011: Voronoi tessellations and their application to climate and global modeling. *Numerical Techniques for Global Atmospheric Models,* P. Lauritzen et al., Eds., Springer, 313–342.

Laprise, R., and Coauthors, 2008: Challenging some tenets of regional climate modelling. *Meteor. Atmos. Phys.,* **100,** 3–22.

Leung, L. R., and Y. Qian, 2003: The sensitivity of precipitation and snowpack simulations to model resolution via nesting in regions of complex terrain. *J. Hydrometeor.,* **4,** 1025–1043.

Li, F., W. D. Collins, M. F. Wehner, D. L. Williamson, J. G. Olson, and C. Algieri, 2011: Impact of horizontal resolution on simulation of precipitation extremes in an aqua-planet version of Community Atmospheric Model (CAM3). *Tellus,* **63A,** 884–892.

Lorant, V., and J.-F. Royer, 2001: Sensitivity of equatorial convection to horizontal resolution in aquaplanet simulations

with a variable-resolution GCM. *Mon. Wea. Rev.,* **129,** 2730–2745.

Mearns, L. O., W. Gutowski, R. Jones, R. Leung, S. McGinnis, A. Nunes, and Y. Qian, 2009: A regional climate change assessment program for North America. *Eos, Trans. Amer. Geophys. Union,* **90,** 311.

Meehl, G. A., and Coauthors, 2007: Global climate projections. *Climate Change 2007: The Physical Science Basis.* S. Solomon et al., Eds., Cambridge University Press, 747–846.

Mishra, S. K., M. A. Taylor, R. D. Nair, P. H. Lauritzen, H. M. Tufo, and J. J. Tribbia, 2011: Evaluation of the HOMME dynamical core in the aquaplanet configuration of NCAR CAM4: Rainfall. *J. Climate,* **24,** 4037–4055.

Mitas, C. M., and A. Clement, 2005: Has the Hadley cell been strengthening in recent decades? *Geophys. Res. Lett.,* **32,** L03809, doi:10.1029/2004GL021765.

Nastrom, G. D., and K. S. Gage, 1985: A climatology of atmospheric wavenumber spectra of wind and temperature observed by commercial aircraft. *J. Atmos. Sci.,* **42,** 950–960.

Neale, R. B., and B. J. Hoskins, 2000a: A standard test for AGCMs including their physical parametrizations: I: The proposal. *Atmos. Sci. Lett.,* **1,** 101–107.

——, and ——, 2000b: A standard test for AGCMs including their physical parametrizations. II: Results for the Met Office Model. *Atmos. Sci. Lett.,* **1,** 108–114.

——, and Coauthors, 2010: Description of the NCAR Community Atmosphere Model (CAM 4.0). NCAR Tech. Note NCAR/TN-485+STR, 212 pp.

O'Gorman, P. A., and T. Schneider, 2007: Recovery of atmospheric flow statistics in a general circulation model without nonlinear eddy–eddy interactions. *Geophys. Res. Lett.,* **34,** L22801, doi:10.1029/2007GL031779.

Oort, A. H., and J. J. Yienger, 1996: Observed interannual variability in the Hadley circulation and its connection to ENSO. *J. Climate,* **9,** 2751–2767.

Park, S.-H., W. C. Skamarock, J. B. Klemp, L. D. Fowler, and M. G. Duda, 2013: Evaluation of global atmospheric solvers using extensions of the Jablonowski and Williamson baroclinic wave test case. *Mon. Wea. Rev.,* in press.

Rauscher, S. A., A. Seth, J.-H. Qian, and S. J. Camargo, 2006: Domain choice in an experimental nested modeling prediction system for South America. *Theor. Appl. Climatol.,* **86,** 229–246.

——, E. Coppola, C. Piani, and F. Giorgi, 2010: Resolution effects on regional climate model simulations of seasonal precipitation over Europe. *Climate Dyn.,* **35,** 685–711.

Ringler, T. D., L. Ju, and M. Gunzburger, 2008: A multiresolution method for climate system modeling: Application of spherical centroidal Voronoi tessellations. *Ocean Dyn.,* **58,** 475–498.

——, J. Thuburn, J. B. Klemp, and W. C. Skamarock, 2010: A unified approach to energy conservation and potential vorticity dynamics for arbitrarily-structured C-grids. *J. Comput. Phys.,* **229,** 3065–3090.

——, D. Jacobsen, M. Gunzberger, L. Ju, M. Duda, and W. Skamarock, 2011: Exploring a multiresolution modeling approach within the shallow-water equations. *Mon. Wea. Rev.,* **139,** 3348–3368.

Seth, A., and F. Giorgi, 1998: The effect of domain choice on summer precipitation simulation and sensitivity in a regional climate model. *J. Climate,* **11,** 2698–2712.

Skamarock, W. C., 2004: Evaluating mesoscale NWP models using kinetic energy spectra. *Mon. Wea. Rev.,* **132,** 3019–3032.

——, 2011: Kinetic energy spectra and model filters. *Numerical Techniques for Global Atmospheric Models,* P. H. Lauritzen et al. Eds., Springer-Verlag, 495–512.

——, J. B. Klemp, J. Dudhia, D. O. Gill, D. M. Barker, X.-Y. Huang, W. Wang, and J. G. Powers, 2008: A description of the Advanced Research WRF version 3. NCAR Tech. Note NCAR/TN-475+STR, 113 pp.

Takahashi, Y. O., K. Hamilton, and W. Ohfuchi, 2006: Explicit global simulation of the mesoscale spectrum of atmospheric motions. *Geophys. Res. Lett.,* **33,** L12812, doi:10.1029/2006GL026429.

Taylor, M. A., J. Edwards, and A. St. Cyr, 2008: Petascale atmospheric models for the Community Climate System Model: New developments and evaluation of scalable dynamical cores. *J. Phys. Conf. Ser.,* **125,** 012023, doi:10.1088/1742-6596/125/1/012023.

Thuburn, J., T. D. Ringler, W. C. Skamarock, and J. B. Klemp, 2009: Numerical representation of geostrophic modes on arbitrarily structured C-grids. *J. Comput. Phys.,* **228,** 8321–8335.

Wheeler, M., and G. N. Kiladis, 1999: Convectively coupled equatorial waves: Analysis of clouds and temperature in the wavenumber–frequency domain. *J. Atmos. Sci.,* **56,** 374–399.

Williamson, D. L., 2008a: Convergence of aqua-planet simulations with increasing resolution in the Community Atmospheric Model, version 3. *Tellus,* **60A,** 848–862.

——, 2008b: Equivalent finite volume and Eulerian spectral transform horizontal resolutions established from aqua-planet simulations. *Tellus,* **60A,** 839–847.

——, and J. G. Olson, 2003: Dependence of aqua-planet simulations on time step. *Quart. J. Roy. Meteor. Soc.,* **129,** 2049–2064.

——, J. Drake, J. Hack, R. Jakob, and P. Swarztrauber, 1992: A standard test set for numerical approximations to the shallow water equations in spherical geometry. *J. Comput. Phys.,* **102,** 211–224.

Zhang, G. J., and N. A. McFarlane, 1995: Role of convective-scale momentum transport in climate simulation. *J. Geophys. Res.,* **100,** 1417–1426.